Phase transformations in low-alloy steel laser deposits

Haitham El Kadiri [a,*], Liang Wang [a], Mark F. Horstemeyer [a], Reza S. Yassar [b], John T. Berry [c],
Sergio Felicelli [c], Paul T. Wang [a]

[a] *Center for Advanced Vehicular Systems, Mississippi State University, Mississippi State, MS 39762, United States*
[b] *Mechanical Eng-Eng Mechanics Department, Michigan Technological University,*
1400 Townsend Drive, Houghton, MI 49931, United States
[c] *Mechanical Engineering Department, Mississippi State University, Mississippi State, MS 39762, United States*

Abstract

We examined the microstructure evolution in medium-carbon low-alloy steel upon laser engineering net shape (LENS) (LENS is a trademark of Sandia National Laboratories and the US Department of Energy, Albuquerque, NM). Involved was the deposition of 14 superimposed fine layers. Several characterization techniques such as scanning electron microscopy (SEM), transmission electron microscopy (TEM), nanoindentation and electron back scattered diffraction (EBSD) were used in conjunction with three-dimensional finite element thermal modeling to rationalize the transformation mechanisms. Delta ferrite was the primary phase to solidify from the melt. Solid-state austenitisation led to allotriomorphic hexagonal prisms that grew following a unique direction depending upon the parent delta-grain crystallographic orientation. A supersaturated lower bainitic plate was the main phase to have transformed from austenite, except for the first two deposited layers where martensite predominated. The supersaturated plate underwent a sudden-tempering reaction at the 10th layer but was confined at the plate boundaries. This tempering reaction became more transgranular and increasingly affected retained austenite and microphases for the underlying layers. Coalescence of carbon-depleted ferrite plates gave rise to the steady-stage microstructure at the fourth layer. This complicated microstructural evolution corroborated the microhardness fluctuations through all deposited layers.
Published by Elsevier B.V.

Keywords: Laser deposition; Low-alloy steel; Bainite; Martensite; SEM; TEM

1. Introduction

A large class of metal alloys has been used to fabricate parts with the laser engineered net shaping (LENS) process [1]. These materials include low-alloy steels [2], stainless steels [3,4], nickel-based alloys [5,6], and titanium alloys [7,8]. Recent advances in system capabilities, thermal modeling, measurement, and processing parameters have succeeded to a certain extent in overcoming the inherent constraints related to net shaping with LENS [9–11]. However, most structural components are multi-phase-based alloys. This makes them highly sensitive to cooling rates. Because of the very high cooling rates associated with laser deposition, the processing window for multi-phase generation is substantially constricted. For steels, the finely generated austenite grain size leads to a high density of allotriomorphic ferrite strings, and the mostly diffusionless transformations generate phases containing high solid solution concentrations. The high fractions of allotriomorphic ferrite strings and solid solution elements lead to very brittle microstructures. To recover some acceptable properties, modern designers resorted to post-mortem heat-treatment processes. These post-tempering processes induced tempering embrittlement problems, increased the cost and labor in the overall manufacturing cost, and eliminated the possibility of obtaining gradients of microstructures.

Because of the complicated relationship between the process parameters and the resulting microstructure, phase and composition modulations in LENS-processed steels were largely neglected. This lack of understanding is a substantial barrier against the development of novel methodologies to better control the microstructure and design of multifunctional alloys.

In this paper, we attempt to thoroughly explain the microstructural and property gradients observed along a single-walled deposit (SWD) from a pre-alloyed AISI 4140 graded steel

* Corresponding author. Tel.: +1 662 325 5568; fax: +1 662 325 5433.
E-mail address: elkadiri@cavs.msstate.edu (H. El Kadiri).

powder. These microstructural gradients were characterized in conjunction with finite element based thermal simulations using SysWeld.

2. Experimental

The SWD or "rib-on-web" builds [12] were manufactured at the Center for Advanced Vehicular Systems (CAVS) using an Optomec machine, but also at Optomec Inc. (Albuquerque, NM). The 14 superimposed fine layers of the SWD were made one layer at a time by injecting powdered metal into the molten puddle created by a laser beam. A high-power YAG laser beam was focused to a fine point on the surface of an AISI 4140 steel substrate creating a molten puddle. The line thickness and width were 0.8 mm and 1 mm, respectively. The laser speed and power were chosen to be 0.89 m/min and 900 W, respectively, so as to melt approximately the half volume of the underlying line. The microstructure was examined by means of Zeiss optical microscope and field emission gun-scanning electron microscopy

(FEG-SEM) on polished samples etched with a 2% diluted solution of "Nital". For transmission electron microscopy (TEM) analyses, 3-mm diameter disks were first extracted by punching a SWD that was previously polished on both sides down to 100 μm. After individual polishing of these disks down to approximately 50 μm, the obtained thin foils were single-jet electro-polished and ion-milled using a Fishionne system. The electropolishing solution was a 2% diluted Nital. FEG-TEM observations were carried out on a 200 keV JEOL instrument. Depth-sensing microhardness tests were performed using a Hysitron multi-range probe nanoindentation system. A maximum load of 1000 mN was applied and relaxed at a rate of 30 mN/s without dwelling time.

3. Overall microstructural variation through the deposits

Fig. 1 shows optical micrographs of typical Nital-etched microstructures for each of the 14 layers.
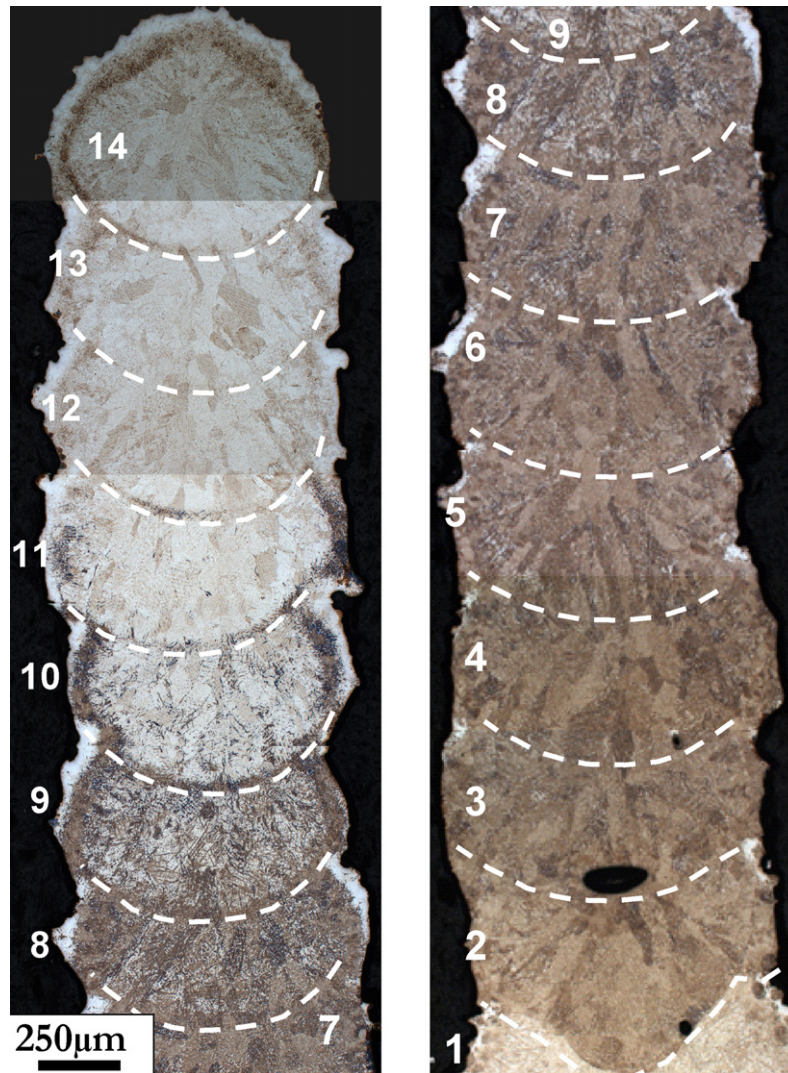

Fig. 1. Optical micrographs of Nital-etched microstructures viewed from sections perpendicular to the laser track corresponding to layers from 1 to 14; note the sudden onset of darkening at the 10th layer, which increases toward the bottom layers, a change in the etching aspect, and a preferential pore formation at layers 1 and 2.
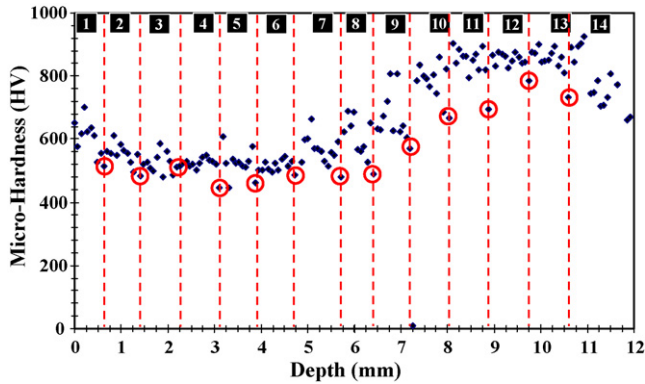
Fig. 2. Hardness along a single profile crossing the entire single-walled deposit obtained from depth-sensing microindentation tests using a maximum load of 1000 mN and relaxation rate of 30 mN/s, without dwelling time. The dashed lines mark the interfaces between layers labeled in sequence from 1 to 14 at the top of the graph, and encircle points correspond to indentations at these interfaces, which showed locally the lowest microhardness bounds.

The most manifest feature from Fig. 1 is the blackening aspect in surface needle-lime morphology that suddenly started at the 10th layer and progressively increased toward the underlying layers. At the eighth layer, this blackening invaded the whole structure.

4. Microhardness

Depth-sensing microindentation tests were performed to reveal the effect of microstructure variation on the mechanical properties. Fig. 2 shows the results of microhardness measurements along a profile running over all 14 layers. The four top layers exhibited the highest microhardness; approximately 930 HV. The microhardness progressively fell beginning at the 10th layer, which corresponded to the first observable outset of the dark-etched structure. The lowest value 500 HV of all microhardness measurements was reached at the sixth layer, which correlated with the first significant appearance of the dark-etched structure. However, the microhardness started slightly increasing through the following underlying layers up to 700 HV reached at the bottom of the first deposited layer. For each layer, the lowest microhardness value was obtained at the fusion interface, where the dark needles were preferentially formed.

5. Thermal analyses

To understand the microstructure evolution through the deposition process, the thermal history of each layer was quantified. A three-dimensional finite element model was developed to simulate the LENS deposition of a SWD using the process parameters given in Section 2. The model and the simulation routines were fully described in [13]. The finite element calculations take into account temperature-dependent material properties and phase transformations. The model generated results which were in a good agreement with the experimental data generated by Hofmeister et al. [15]. Fig. 3a depicts the thermal cycles at the mid-point of all deposited layers. Each peak indicated that the laser beam passed nearly over the pre-defined location, from initial layer to subsequent deposited layers. The peak tempera-
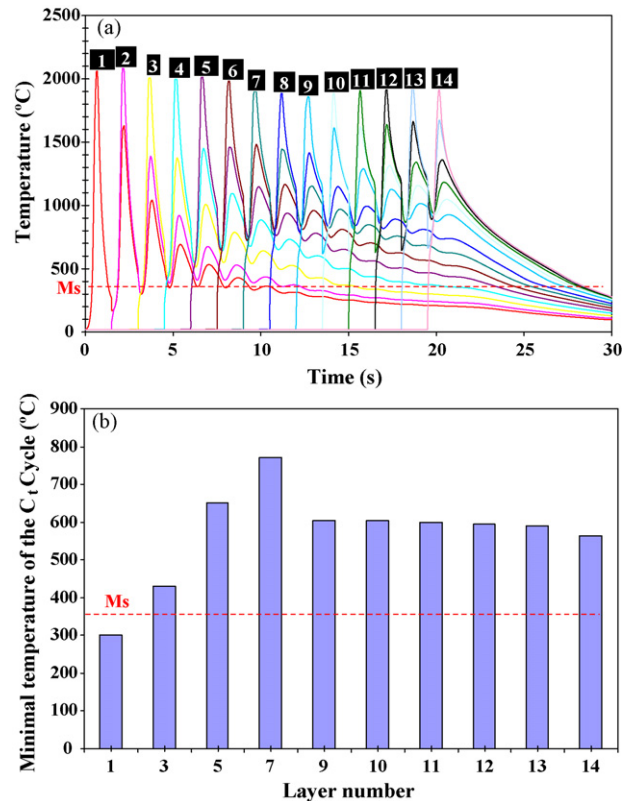

Fig. 3. (a) The thermal history of the single-walled deposit calculated at the mid-point of each deposited layers by finite element simulations using a three-dimensional model that was developed as a subroutine in the SYSWELD software tool [13], and (b) the minimum temperature of C_t cycle immediately following the last melting cycle for each layer in comparison with the martensitic starting temperature (350 °C).

ture progressively decreased for the subsequent deposited layers [16]. The minimum temperature of the cycle, denoted C_t, immediately succeeding the last melting cycle of each layer varied along the deposition (Fig. 3b). Since the duration of each cycle following the C_t cycle was only in the range of 1 s or less, the re-austenitisation amplitude in solid state would be negligible. As such, the displacive phases that formed following the C_t cycle were undissolved, except for a possible tempering reaction. Note that for all layers between 3 and 14, this temperature was greater than the martensitic starting temperature ($M_s = 350$ °C) (Fig. 3b).

6. Microstructure at the top layer (14th layer)

In the following, we first present the microstructure at the two top layers. The microstructure is a key to understanding the process effect, since it is in principle the initial microstructure generated in the as-deposited condition for all layers, except for the two first.

6.1. Grain structures of δ-ferrite and γ-austenite

The solidification consisted of the epitaxial nucleation [17] of large columnar delta-ferrite grains (Fig. 1). Fig. 4a evidences direct nucleation of γ-allotriomorphs at the former δ-ferrite grain boundaries. The daughter γ was distinguished from the mother
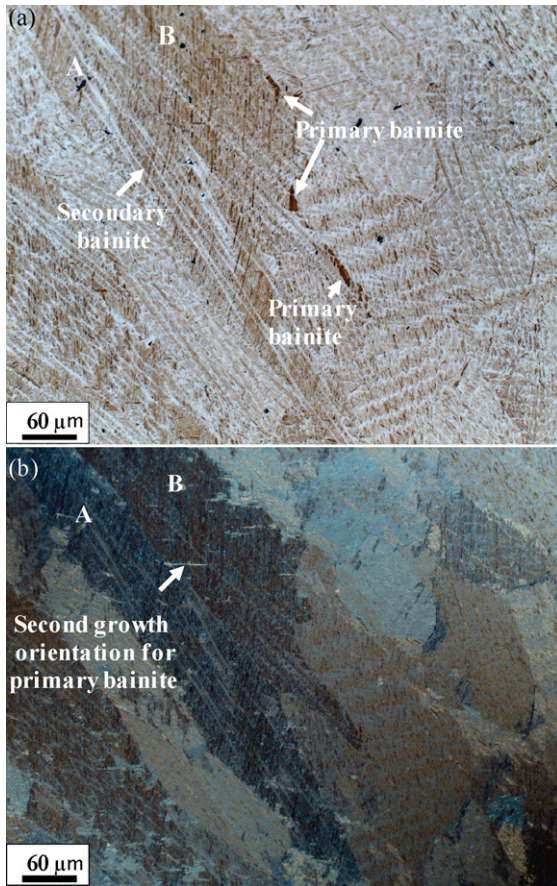
Fig. 4. Optical micrographs revealing the dependency of γ-prism main axis direction on the crystallographic orientation of the former δ-grains showing (a) few apparent morphologies of γ-prisms in the same region of layer 14, and (b) a differential contrast interference image of the same region exposing the texture of the former δ-grains corroborating a unique γ-prism orientation in a single parent δ-grain. The crystallographic orientation was slightly different between grains noted A and B and accordingly, the corresponding γ-prisms nodules and bainite sheaves were slightly rotated.

δ-ferrite crystals by a discontinuous intergranular precipitation of allotriomorphic ferrite (α_a) decorated by cementite particles. Intergranular cementite and iron-chromium rich particles were identified via energy-dispersive X-ray spectrometry (EDS) and electron back-scatter diffraction (EBSD) coupled mapping in Fig. 5. The allotriomorphic ferrite was substantiated by the isotropic thickening on both sides of the γ-boundaries [16]. As illustrated in Fig. 4a, the γ-cells exhibited a morphology that can appear equiaxed or elongated by regions. Bhadeshia and co-workers demonstrated in [18,19] that because of the cellular nature of the solidification front, the γ-allotriomorphs can be represented by space filling hexagonal prisms of length "c" and cross-sectional side length "$L/2$", where $c \gg L$. As such, the apparent equiaxed microstructure should correspond to more or less an axial view of these elongated hexagonal prisms. However, the authors observed that the γ-prisms were exclusively extended along the transverse direction. Therefore, they attributed this morphology to an anisotropic growth due to a thermal gradient effect. Nonetheless, the differential interference contrast (DIC) type optical images in Fig. 4a clearly evidence that the orien-

tation distribution of γ-allotriomorph prisms varied by zones that corresponded to the former δ-ferrite grains. The growth orientation of the elongated γ-prisms depended in fact on the crystallographic orientation of the parent δ-ferrite grain.

6.2. Primary lower bainite

Fig. 6a demonstrates nucleation of thick and long phases in plate-like morphology directly on a former δ-grain boundary, which was completely free of α_a. These side-plates radiated from the former δ-grain boundaries sporadically and exclusively grew confined in only one side of the apparent δ-grain. This growth confinement indicated a displacive controlling mechanism and not a reconstructive transformation [20]. A closer view of these side-plates in TEM and SEM evidenced a cluster of ferrite sub-units separated by an extremely fine layer of retained austenite (Fig. 7a). A TEM dark-field image of a typical cementite spot in a selected-area diffraction (SAD) pattern reveals a small extent of nano-sized carbide precipitation (Fig. 7b). The inverse pole figure grain orientation maps (Fig. 5a) show a noticeable continuous orientation change in each single alpha grain. This typically indicates a highly dislocated structure. The cluster of parallel and highly dislocated subunits enclosing nano-carbides is a structure reminiscent of lower bainite.

We adopted the terminology primary lower bainite (denoted here α'_b) on the grounds that this phase nucleated at a former δ-grain boundary. To our knowledge, a similar phase with this distinguishing nucleation feature has never been reported in the literature. Another distinguishing feature of α'_b was the large sheave width that can be reached along the prior δ-grain boundary, typically 20–30 μm. As evidenced by Fig. 6a, α'_b can extend across several γ-prisms or remain confined within a single one. When crossing several γ-prisms, the width of α'_b seemed to shrink down each time a γ-prism boundary was encountered. The growth of α'_b occurred along two orientations almost perpendicular to each other, but one was more preponderant than the other. When both orientations nucleated tail-to-tail at the same δ-boundary segment, the sheaves gave the appearance of a butterfly-like morphology (Fig. 8a) previously reported in the literature [21]. Close to the fusion boundary, α'_b tended to increasingly adopt the form of the classical bainite variant (Fig. 8b). The classical lower bainite was distinguished by carbide precipitation in and in-between the bainitic ferrite platelets.

6.3. Secondary lower bainite and retained austenite

Between two adjacent γ boundaries, secondary displacive nodules (α_b), reacting exactly similarly to the etching agent as α'_b, grew as parallel sheaves with a width scarcely exceeding 2 μm (Fig. 9a and b). They are attributed to secondary lower bainite (α''_b). These secondary lower bainite sheaves formed at the γ-prism boundary segments that were not subjected to a noticeable α_a precipitation. The interspacing between the sheaves was slightly smaller than a typical width of an individual sheave. In this interspace (Fig. 11b), less-marked etching-induced darkening was systematic, and suggested a mixture of retained austenite and microphases undergoing less extent of carbide precipitation
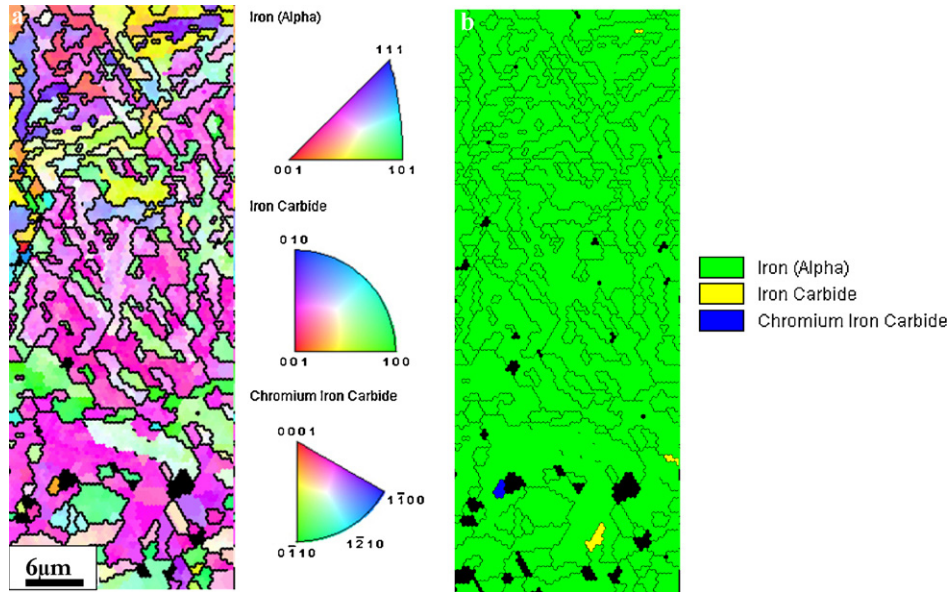
Fig. 5. Electron back-scatter diffraction analyses of portion of layer 13 illustrating (a) a highly dislocated structure in the inverse pole figure grain orientation map, and (b) the nature of carbides in the phase map.
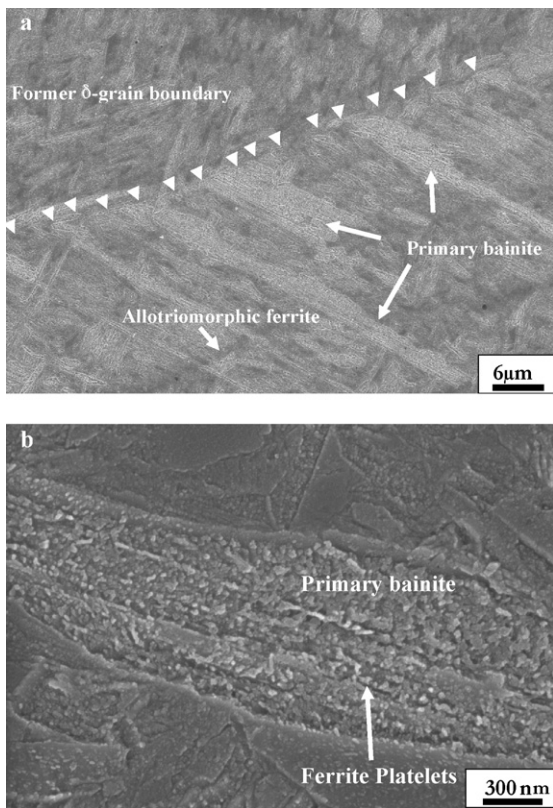

Fig. 6. SEM micrographs of Nital-etched samples revealing (a) primary bainite plates in layer 13 extending through several γ-prisms after direct nucleation on a single side of a former δ-grain boundary, and (b) high magnification images of a typical primary bainite in layer 13 revealing extremely fine supersaturated ferrite platelets.
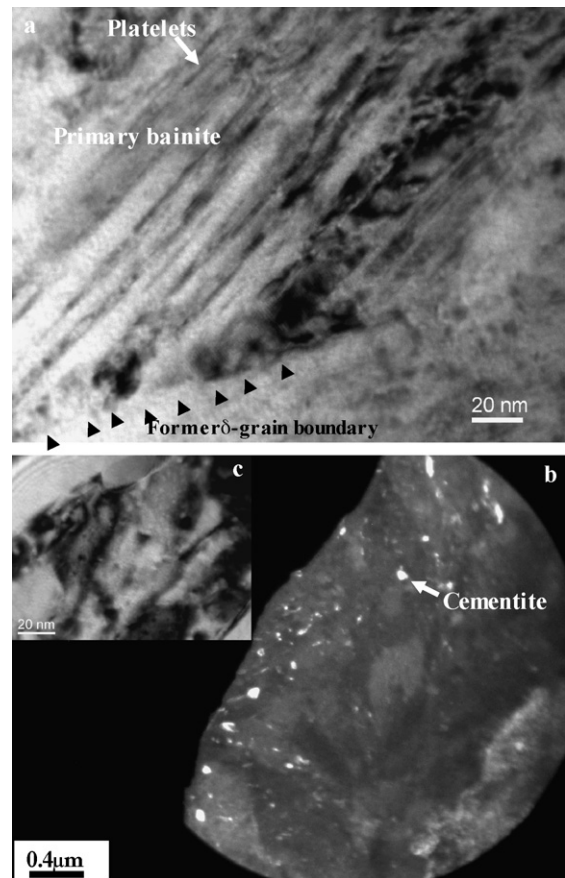

Fig. 7. TEM analyses showing (a) a bright-field image of primary lower bainite revealing extremely thin ferrite plates, with a thickness in the order of 5–10 nm, separated by extremely small film of retained austenite, and (b) a dark-field image corresponding to a typical spot of cementite in the bright-field of image (c), revealing small extent of carbide precipitation.
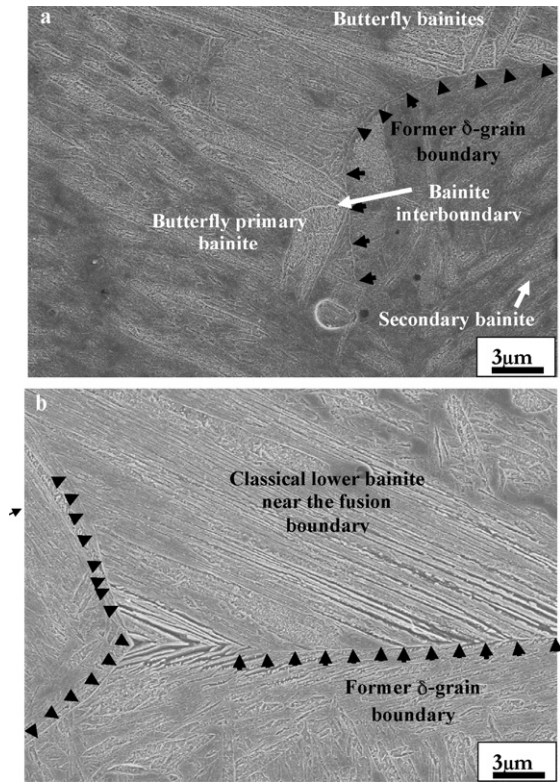
Fig. 8. SEM images of Nital-etched samples revealing (a) coexistence of two growth orientations in layer 13 forming a butterfly-like structure when two sheaves are nucleated at the same former δ-grain segment, and (b) precipitation of the classical form of primary lower bainite nucleated at a former triple δ-boundary junction in the fusion line between layers 14 and 13.

Fig. 9. (a) A SEM image of Nital-etched microstructures in layer 13 revealing precipitation of secondary lower bainite sheaves within γ-prism polygons with different crystallographic orientation having reacted differently to the etching agent, and (b and c) an optical micrograph of Nital-etched microstructure in layer 10 revealing the sudden onset of tempering reactions at that layer with exclusive precipitation of carbides at the intergranular regions and along the spinal line for some sheaves suggesting the presence of martensitic mid-rib.

as suggested in [22]. Figs. 6a and 7a show that the α''_b growth orientations depended upon the former delta grain orientations in which the parent γ-prisms grew. For all γ-prisms confined in a single former delta grain, the α''_b adopted the same growth orientations. This phenomenon indicates that the crystallographic texture of this parallel γ-prism packet depended on the crystallographic orientation of the parent δ-grain. This is an important finding that to our knowledge is not reported in the literature.

7. Microstructure evolution in the LENS deposit

Layers 11–13 exhibited nearly the same kind of microstructure, indicating that the consecutive deposition did not induce any changes on the three underlying layers. There is, however, a difference between layer 14 and the three underlying layers that will be discussed further. As mentioned above, the first change in the microstructure was observed at the 10th layer (Fig. 1). In this layer, the dark etching in surface needle-like shape corresponded to the formation of carbides at the exterior boundaries of α'_b and α''_b (Fig. 9b and c). These carbides were identified as cementite through TEM analyses. Some plates showed also a fine precipitation along a spinal line of the phase (Fig. 10a and b). The tempering reaction at the 10th layer affected preferentially α'_b and was sporadic for α''_b. The extent of coarsening progressively increased to invade basically all bainite sheaves and retained austenite blocks at the fourth deposited layer (Fig. 12a and b).
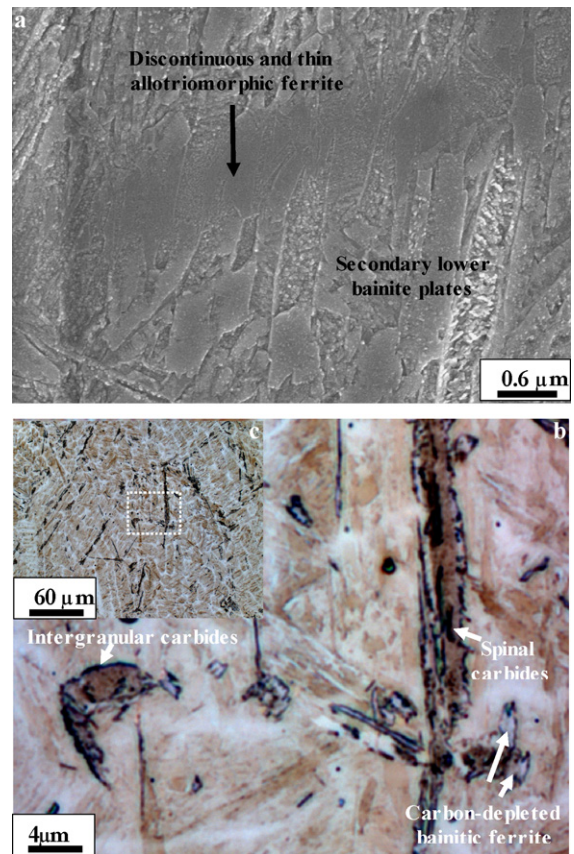
Within an individual sheaf, the coarsening became increasingly transgranular from as sooner as layer 8. The carbides tended to coarsen as surface needle-shaped morphology aligned along the former plate boundaries. However, within the plate, increasing number of carbide particles were observed to be inclined about 60° with respect to the plate boundary (Fig. 10a). When the sheaf showed a pair of spinal boundaries, the tempering led to spherical carbides (Fig. 10b). A later stage of microstructure evolution is illustrated in Fig. 11a. This stage corresponded to the coalescence of several tempered α'_b and α''_b sheaves and coarsening of α_a. At layer 7 and below, the carbide-free bainitic ferrite started coalescing with α_a (Fig. 11b). The coalescence occurred along the direction of the carbide-free bainitic subunits. At layer 4, this phenomenon gave rise to the steady-state microstructure, which consisted of an apparent equiaxed microstructure of γ-grains even at cross-sections cut parallel to the γ-prism main axis (Fig. 12a). A thick layer of ferrite formed a honeycomb-like structure within the former δ-grain. Within each cell of this honeycomb structure, parallel surface needles of carbides aligned in a carbon-depleted ferrite matrix.

For the first and second deposited layers, Fig. 12b shows the presence of carbide-free rectangular-like zones decorated by a
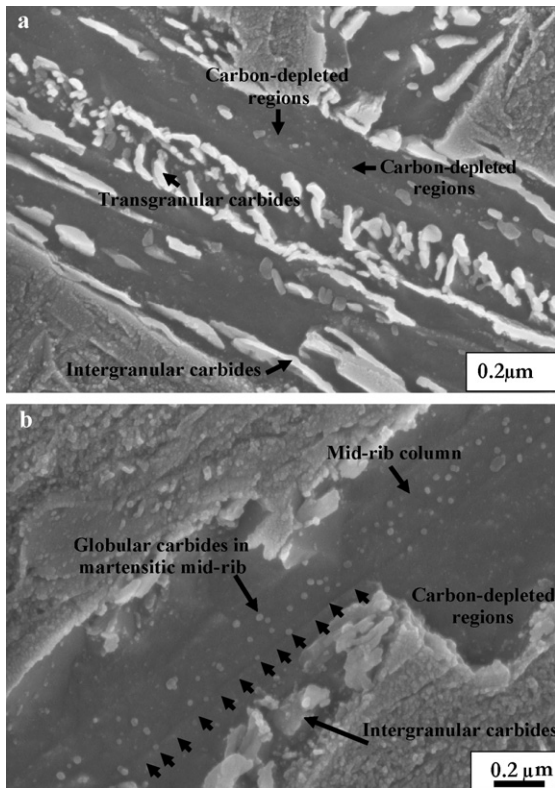
Fig. 10. SEM images of Nital-etched microstructures in layer 8 revealing a substantial tempering within a plate exposing alignment of intergranular carbides parallel to the plate boundary and of transgranular carbides along about 60° with respect to the main axis of the plate, and (b) a fully tempered secondary lower bainitic sheave with potentially a martensitic mid-rib in twinning-like shape exhibiting globular carbides exclusively located between the two spinal boundaries.
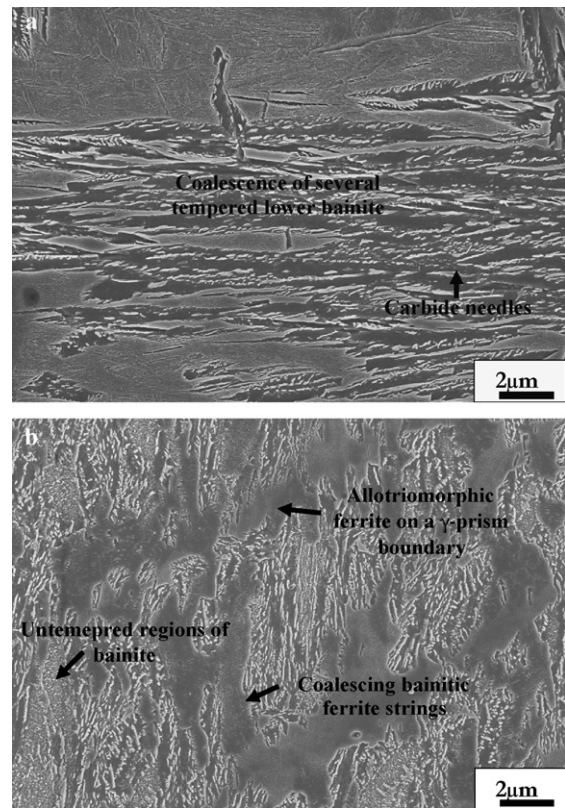

Fig. 11. SEM images of Nital-etched microstructures revealing (a) in layer 7 coalescence of many primary and secondary bainite sheaves trapping elongated colonies of untempered retained austenite and microphases, and (b) the formation in layer 6 of large carbon-free bainitic ferrite that tended to coalesce with allotriomorphic ferrite along a unique direction for each former δ-grain corresponding to the former sheave boundary, some of the secondary sheave were scarcely still untempered.

network of twinning-like structures. These precipitates may correspond to martensite side-plates confined within impingement zones of different bainite sheaves [23,24]. These martensite nodules can even form between single sub-units belonging to two distinct sheaves.

8. Discussion

It was revealed on etched microstructures that the δ-grains were columnar in nature and extended along that direction to approximately 450 μm away. A typical width of the δ-ferrite grains was 100 μm, which increased to approximately 250 μm for the three first deposited layers. Bhadeshia et al. [18] carried out stereological measurements on two chemically different low-alloy steel weld deposits using three oriented sections. These three sections were transverse, longitudinal, and 45° inclined with respect to the weld center line. The authors concluded that the γ-grain structure can be represented as a honeycomb of elongated hexagonal prisms. The authors stated that the γ-grains appeared elongated in the transverse direction normal to the temperature isotherms, and equiaxed in the longitudinal section. They further stated that this morphology was consistent with a cellular solidification, in which the solid–liquid interface consisted of a honeycomb structure. However, these authors

used a low-alloy steel that solidified with δ-ferrite as the primary phase, as they stated further in their paper. As such, the austenitisation rather occurred in solid state. In this study, we clearly demonstrated that the elongation of γ-prisms was not necessarily normal to the temperature isotherms as stated by Bhadeshia et al. [18]. The gamma grains were all elongated, but their geometric orientation depended on the crystallographic orientation of the parent δ-grain. All γ-prisms boundaries confined within a single δ-grain exhibited a unique orientation.

The formation of α_a has substantial influence on subsequent transformations within the γ-prisms. The extent of this phase at the γ-prism boundaries is such that it can either bias or promote certain displacive phases over others [17–26]. It has been long believed that α_a forms a continuous layer along the γ-prism boundaries. In some heavily alloy welds, however, discontinuous layer of α_a was observed [27]. This motivated Bhadeshia et al. to consider growth phenomena prior to site saturation [28]. Due to the very high cooling rates associated with the laser melting, the low-alloy steel deposits showed fine α_a-allotriomorphs that sporadically covered the γ-prism boundaries.

The allotriomorphic ferrite was nonetheless completely absent from the former δ-grain boundaries. This is an intriguing behavior that has not been reported in the literature. α_a is rather expected since the former δ-grain boundary became basically
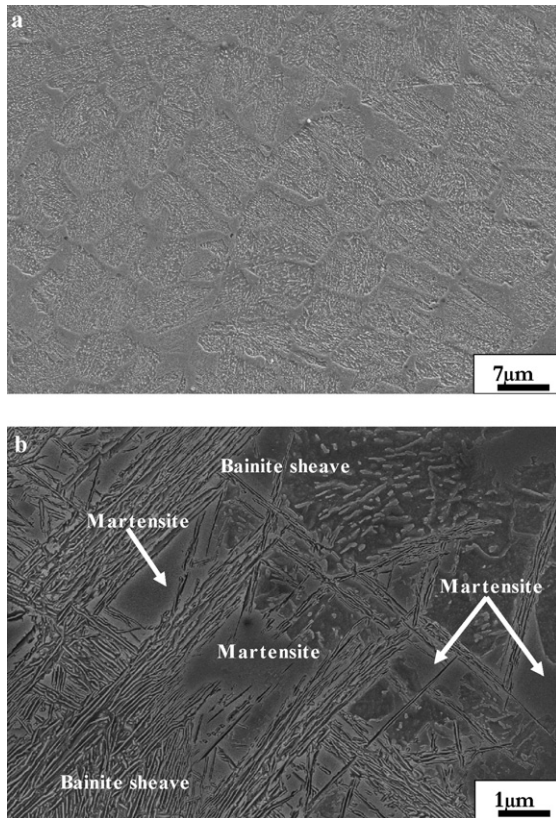
Fig. 12. SEM images of a Nital-etched microstructure depicting (a) the final stage of microstructure in layer 4 consisting of a network of apparent equiaxed γ-grain resulting of coalescence between allotriomorphic ferrite and carbon-free bainitic ferrite, and carbide alignments within each apparent former γ-grain, and (b) martensitic plates in layer 1 formed at impingement zones of several well-tempered primary lower bainite sheaves.

a γ-grain boundary, after the austenitic γ-allotriomorphs have formed on both sides. Several γ-grains coexisted on both sides along a single segment of the former δ-boundary. As such, the grain misorientation level should vary along each single segment. This misorientation variation gave rise to inhomogeneous interfacial properties along a single former γ-segment. As such, it may have played a role in inhibiting nucleation and/or growth of α_a-allotriomorphs.

The austenite grains were subjected to an important precipitation of brown-etched sheaves identified here as variants of the lower bainite phase (α_b), and not martensite (α'). These sheaves sometimes exhibited a fine central spine revealed after tempering reaction, which can be attributed to a martensitic midrib [29]. When the α'_b nucleated at a γ-grain segment, formerly a δ-grain boundary, the resulting sheave was larger, and colonies of butterfly morphology were formed. The brown sheave was identified as α_b based upon several arguments:

(1) First, the possibility of widmanstätten ferrite (α_w) is to be excluded here. α_w is known to nucleate at the γ/α_w interface. As mentioned above, α_a interfaces did not form at the former δ-grain boundaries, where, however, brown sheaves were formed. Moreover, α_w does not etch as observed in our micrographs.

(2) At first place, and for each layer beside layer 14, the cooling rates from approximately the Ae3 temperature during the first cycle immediately following the last melting cycle, denoted here as C_t cycle, was in the range of 500 K/s. This cycle is of significant importance, since it corresponded to the first episode of possible irreversible solid transformations. According to the CCT diagram of AISI 4140 with 1% of Mn [30,31], this fast cooling rate positions the corresponding cooling curve outside all phase transformation domains till the martensitic domain boundary. This suggests that α' will be the predominant phase to form if any phase transformation had to occur. However, the possibility of ascribing the brown displacive plate to martensite could be undermined by a scrupulous analysis of the calculated thermal history of the SWD. First, martensitic transformation is only thermodynamically possible to occur when the temperature drops below the M_S [30]. However, as illustrated in Fig. 3, only the first and most probably the second layer saw their lower bound temperature of the C_t cycle (T_t), dropped below M_S. If any phase transformation had to occur at that level, the resulting microstructure might unlikely have re-austenitized. In fact, the life time of each thermal spike exceeding the Ae3 temperature hardly surpassed 1 s. For all the 12 top layers, the only time the temperature dropped below the M_S all along the deposition process was when the layer monotonically cooled down to the ambient. We observed, however, at the 10th layer, a sudden onset of cementite precipitation within the brown sheaves. Layer 11 was in point of fact completely free of any tempering reaction evidence. Fig. 3 evidenced that the temperature exposure difference below M_S between layers 10 and 11 was less than 1 s. This extremely short period of exposure time cannot explain the substantial tempering difference between the two layers. As such, the brown sheaves could not be the result of a martensitic transformation.

(3) SEM images at high magnification revealed that the plate exhibited a cluster of parallel and extremely thin plates. This structure corresponded in fact to a highly dislocated α_b-sheave, where a small amount of nano-sized carbides formed within the α_b-ferrite plates. Stark et al. developed in medium carbon steel a structure consisting of a mixture of a supersaturated bainitic ferrite and retained austenite [32]. This structure closely resembles our variant of brown α_b-sheave. On one hand, bright-field TEM images of a typical plate confirmed a cluster of extremely fine and highly dislocated sub-units separated by fine films of retained austenite (Fig. 7). The relatively large dislocation density is in accordance with the classical description of bainite put forward by Bhadeshia [33]. On the other hand, dark-field images of a typical spot of cementite corroborated the precipitation of a small amount of nano-sized cementite particles as observed in the SEM images. HREM images of Fig. 13a and b demonstrate that a typical cementite particle was few nanometers thick and contains a faulted structure. Ohmori [34], Nagakura et al. [35] and Nakamura et al. [36] attributed these faults in bainitic cementite to an intergrowth of χ carbides and cementite. This intergrowth, which was then
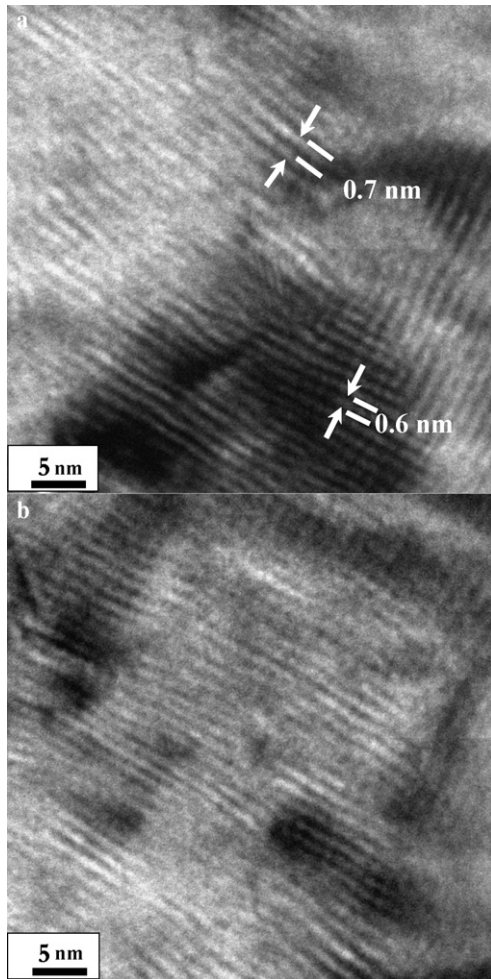
Fig. 13. Lattice-resolution transmission electron micrographs of carbides revealing (a) the existence of two types of lattices that may correspond to an intergrowth between cementite and χ-carbides, and (b) precipitation of carbides at the dislocation tangles.

described as microsyntactic intergrowth led to a nonstoichiometric overall composition expressed by $Fe_{2n+1}C_n$, where $n \geq 3$. The intergrowth of χ carbides and cementite supported the great similarities between tempered α' and α_b as discussed by Bhadeshia in [37]. The limited extent of cementite precipitation in α_b can be rationalized through the tempering theory put forward by Kalish and Cohen [38]. These authors showed that carbon atoms are energetically promoted to remain segregated at dislocations when compared with their presence in a metastable carbide lattice such as in ε-carbide. If the dislocation density is sufficiently high, the carbon will not be available for carbide precipitation. Bhadeshia showed that this carbide precipitation retardation was exacerbated in high-silicon medium carbon steel [39,40]. This effect is to be highly expected in our SWD which was based on high-silicon medium carbon steel having in fact a higher concentration of silicon. Similarly, Kang et al. [41] observed via in situ hot-stage TEM that lower bainitic ferrite remained supersaturated with carbon some noticeable time after the completion of the ferrite growth. This could be augmented by the high

cooling rates associated with the laser deposition. The most intriguing phenomenon about the formation of α_b is the direct ramification of the aforementioned argument number 2. The α_b observed in layers 3–13 must have formed in fact during the C_t cycle. This cycle atypically remained above M_S and showed a cooling rate in the range of 500 K/s (Fig. 3b). As such, when plotted in the CCT diagram, no phase transformation is predicted to occur. As such, our previous argument implies a deficiency of current CCT diagrams. To our knowledge, no available data on phase transformation were reported for a thermal cycle similar to the C_t cycle.

The only noticeable difference in terms of thermal history between layers 10 and 11 is an additional cycle experienced by layer 10. This cycle has a peak temperature of approximately 1050 °C and time amplitude of 0.75 s. In an effort to appreciate the difference in terms of time–temperature exposures between layers 10 and 11, we reported in Fig. 14 the average temperature experienced by each of these layers for a period of time of approximately 6 s after solidification. The 6 s corresponded factually to the life time of the cycling period for layer 10 starting from the C_t cycle and ending up at the beginning of the monotonic cooling to the ambient. The average temperature for this period of time was approximately 1082 °C for layer 10 and 930 °C for layer 11. Knowing the thermally activated nature of tempering reactions, a temperature difference of 150 K could more rationally make the difference in the observed mismatch amplitude of carbide precipitation observed between these two layers. This finding substantiates the formation of bainite during the C_t cycle and not during cooling down to the ambient.

It is noteworthy that the drop of hardness also at the first layer corroborates the above argument for α_b identification. The first layer cooled down directly monotonically to room temperature. As such, the degree of supersaturation would be lower than in the underlying layers. The solid solution induced hardening will be then less noticeable.

The carbide precipitation at the plate boundaries occurring at the initial stages of tempering corroborates bainite and not
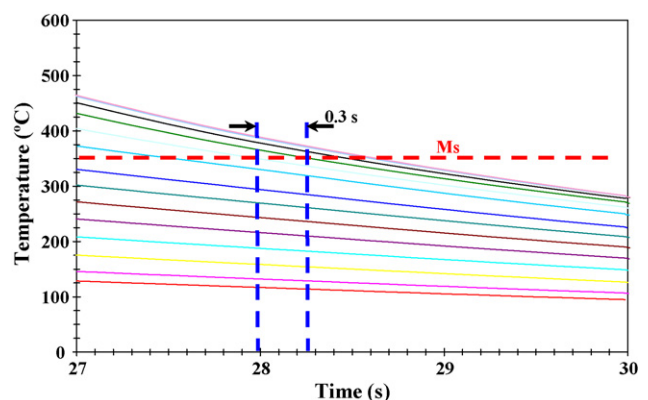

Fig. 14. (a) Temperature profiles at the mid-point of each deposited layer illustrating the small difference in exposure time (0.3 s) between layers 10 and 11 after the temperature dropped monotonically below the martensitic starting temperature for both layers (350 °C).

martensite as suggested in Ref. [42]. However, the spinal precipitation suggests the presence of a martensite mid-rib, given the fact that carbides coarsen much faster in a martensitic mid-rib. The mid-rib formation was observed to occur isothermally at temperatures slightly above M_S [29]. However, the minimal temperature during the C_t cycle remained noticeably above M_S. This phenomenon suggests that the upper bound temperature of the swing back regime, T_r, reported in the literature [43] may depend upon the cooling rates. Okamoto and Oka [44] reported that the difference between T_r and M_S diminishes as carbon content of the steel decreases. This effect is consistent with the high cooling rates associated with the LENS process. Under layer 10, carbide precipitation became progressively transgranular and then affected the neighboring regions. This progressive tempering was concurrently reflected in the microhardness. First a sudden drop of hardness occurred at the 10th layer corroborating the sudden onset of substantial intergranular tempering. The hardness kept falling at the same rates in the underlying layers till a plateau was reached at the top of layer 6. This monotonic drop reflects the monotonic increase in tempering observed for bainite, retained austenite and microphases.

A closer SEM view of a tempered bainitic plate shows that carbide particles had a surface needle-like shape with their longest axes inclined at about $60°$ to the plate boundary. This single crystallographic variant adopted by carbides in a transformed sheave is characteristic of a bainitic matrix and not a martensitic one [45,46]. In martensite, carbides rather exhibit a multi-variant crystallographic precipitation [20].

The redistribution of carbon and the precipitation of carbides in the α_b sheaves and in the neighboring regions induced carbon-free bainitic ferrite colonies. These colonies coalesced with the allotriomorphic ferrite leading to an apparent former equiaxed austenite grain microstructure even in sections parallel to the γ-polygons. At the apparent γ-grain boundaries, continuous strings of carbide-free ferrite dotted with spherical cementite tend to increasingly thicken toward the bottom layers. These apparent grains enclosed a carbon-free bainitic ferrite matrix marked with carbide needle alignments. This constituted a steady-state microstructure. For the first two layers we observed the formation of massive martensite nodules. These martensite nodules contained substantial transgranular carbides. This tempered martensite explained the sudden increase of microhardness measured for the same layers.

9. Conclusions

A complicated phase transformation occurred during laser engineering net shape (LENS[1]) deposition of an AISI 4140 powder into 14 superimposed fine layers. In all layers, columnar prior delta-ferrite grains formed and grew perpendicularly to the fusion interface. Within these grains, allotriomorphic hexagonal austenite prisms grew in a direction that depended on the crystallographic orientation of the parent delta-ferrite grain.

In the four top layers, the austenite allotriomorphs intergranularly transformed to discontinuous and shallow allotriomorphic ferrite. Partial transformation occurred in the austenite prisms into several forms of lower bainite plates, namely a supersaturated bainitic ferrite plate. Retained austenite and micro-phases appeared as intervening colonies between the bainite plates. A lower bainite sheave with a midrib was also observed, and classical lower bainite sheaves were predominant at the fusion line regions. Larger primary lower bainite sheaves were observed to directly nucleate at prior delta-ferrite grain boundaries. At the 10th deposited layer, a noticeable carbide precipitation including metastable forms of cementite took place at the bainite sheave boundaries and midrib regions, and became increasingly more transgranular toward the underlying layers. The tempering reactions increasingly affected the retained austenite and microphases regions. The carbon depletion and carbide precipitation processes increasingly depleted the bainitic ferrite plates. The resulting carbon-free bainitic ferrite coalesced with the allotriomorphic ferrite. An austenite prism was as such subdivided into many apparent equiaxed grains in which carbide surface needles aligned with the former sub-unit boundaries. For the first two deposited layers, martensitic side-plates were more predominant within the austenite allotriomorphs, since the minimum temperature after the last melting cycle dropped below the swing back and martensitic starting temperatures. This complicated microstructural variation during deposition rationalized the observed variations of microhardness through all deposited layers.

Acknowledgments

References

[1] J. Mazumder, H. Qi, Int. Soc. Opt. Eng. 5706 (2005) 38–59.
[2] D.M. Keicher, W.D. Miller, J.E. Smugeresky, J.A. Romero, D.M. Keicher, W.D. Miller, J.E. Smugeresky, J.A. S Romero, Proceedings of the TMS Annual Meeting on Hard Coatings Based on Borides & Carbides & Nitrides: Synthesis Characterization & Application, 1998, pp. 369–377.
[3] J.A. Brooks, T.J. Headley, C.V. Robino, Materials Research Society Symposium—Proceedings 625 (2000) 21–30.
[4] J.A. Brooks, C.V. Robino, T.J. Headley, J.R. Michael, Weld. J. 82 (2003) 51/S–64/S.
[5] W. Liu, J.N. Dupont, Metall. Mater. Trans. A 34 (2003) 2633–2641.
[6] M.L. Griffith, M.T. Ensz, J.D. Puskar, C.V. Robino, J.A. Brooks, J.A. Philliber, J.E. Smugeresky, W.H. Hofmeister, Materials Research Society Symposium 625 (2000) 9–20.
[7] S.M. Kelly, S.L. Kampe, C.R. Crowe, Materials Research Society Symposium 625 (2000) 3–8.
[8] S.M. Kelly, S.L. Kampe, Metall. Mater. Trans. A 35 (2004) 1869–1879.
[9] M.L. Griffith, D.L. Keicher, J.T. Romero, J.E. Smugeresky, C.L. Atwood, L.D. Harwell, D.L. Greene, Am. Soc. Mech. Eng. 74 (1996) 175–176.
[10] W. Hofmeister, M. Griffith, M. Ensz, J. Smugeresky, JOM 53 (2001) 30–34.

---

[1] LENS is a trademark of Sandia National Laboratories and the United State Department of Energy, Albuquerque, NM.

[11] Y. Hu, V.Y. Blouin, G.M. Fadel, Proceedings of SPIE—The International Society for Optical Engineering 5605 (2004) 214–225.

[12] K. Dai, L. Shaw, Acta Mater. 53 (2005) 4743–4754.

[13] L. Wang, S. Felicelli, Mater. Sci. Eng. A 435–436 (2006) 625–631.

[15] W. Hofmeister, M. Wert, J. Smugeresky, J.A. Philliber, M. Griffith, M. Ensz, JOM 51 (1999).

[16] P. Gorman, J.E. Smugeresky, D.M. Keicher, Proceedings of the TMS Fall Meeting, 2002, pp. 167–173.

[17] H.K.D.H. Bhadeshia, L.E. Svensson, B. Gretoft, Acta Metall. 33 (1985) 1271–1283.

[18] H.K.D.H. Bhadeshia, L.E. Svensson, B. Gretoft, J. Mater. Sci. 21 (1986) 3947–3951.

[19] L. Gavard, H.K.D.H. Bhadeshia, D.J.C. MacKay, S. Suzuki, Mater. Sci. Technol. 12 (1996) 453–463.

[20] H.K.D.H. Bhadeshia, D.V. Edmonds, Acta Mater. 28 (1980) 1265–1273.

[21] T.Z. Wozniak, Mater. Sci. Eng. A 408 (2005) 309–316.

[22] D.J. Abson, R.E. Dolby, P.H.M. Hart, Agard Conference Proceedings, vol. 1, 1979, pp. 75–101.

[23] T.N. Durlu, J. Mater. Sci. Lett. 15 (1996) 1412–1415.

[24] R. Villegas, A. Redjaimia, M. Confente, M.T. Perrot-Simonetta, www.msm.cam.ac.uk/phase-trans/2005/LINK/151.pdf.

[25] H.K.D.H. Bhadeshia, L.E. Svensson, B. Gretoft, ASM Int. (1986) 225–229.

[26] H.K.D.H. Bhadeshia, L.E. Svensson, B. Gretoft, J. Mater. Sci. Lett. 4 (1985) 305–308.

[27] H.K.D.H. Bhadeshia, L.E. Svensson, J. Mater. Sci. 24 (1989) 3180–3188.

[28] H.K.D.H. Bhadeshia, L.E. Svensson, B. Gretoft, Proceedings of an International Conference on Welding Metallurgy of Structural Steels, 1987, pp. 517–530.

[29] J. Sun, H. Lu, M. Kang, Metall. Trans. A 23 (1992) 2483–2490.

[30] C.E. Bates, G.E. Totten, R.E. Brennan, ASM Handbook: Heat treating, vol. 4, ASM International, 1991, pp. 67–118.

[31] H.K.D.H. Bhadeshia, Bainite in Steels, Transformation, Microstructure and Properties, The Institute of Materials, London, 1992, p. 173.

[32] I. Stark, G.D.W. Smith, H.K.D.H. Bhadeshia, Metall. Trans. A 21 (1990) 837–844.

[33] H.K.D.H. Bhadeshia, Bainite in Steels, Transformation, Microstructure and Properties, The Institute of Materials, London, 1992, p. 61.

[34] Y. Ohmori, Proceedings of the International Conference on Martensitic Transformations (ICOMAT-86 Nara), Japan Institute of Metals, Sendai, 1986, pp. 587–594.

[35] S. Nagakura, T. Suzuki, M. Kusunoki, Trans. Jpn. Inst. Met. 22 (1981) 699–709.

[36] Y. Nakamura, T. Mikami, S. Nagakura, Trans. Jpn. Inst. Met. 26 (1985) 876–885.

[37] H.K.D.H. Bhadeshia, Bainite in Steels, Transformation, Microstructure and Properties, The Institute of Materials, London, 1992, p. 85.

[38] D. Kalish, M. Cohen, Mater. Sci. Eng. A 6 (1970) 156–166.

[39] S.K. Liu, G.Y. Zhang, Metall. Trans. A 21 (1990) 1509–1515.

[40] H.K.D.H. Bhadeshia, Bainite in Steels, Transformation, Microstructure and Properties, The Institute of Materials, London, 1992, p. 185.

[41] M.K. Kang, J.L. Sun, Q.M. Yang, Metall. Trans. A 21 (1990) 853–858.

[42] W.J. Nam, ISIJ Int. 39 (1999) 1181–1187.

[43] M. Oka, H. Okamoto, Metall. Trans. A 19 (1988) 447–452.

[44] H. Okamoto, M. Oka, Metall. Trans. A 17 (1986) 1113–1120.

[45] K.J. Irvine, F.B. Pickering, JISI 188 (1958) 101–115.

[46] G.R. Speich, Decomposition of Austenite by Diffusional Processes, Interscience, New York, NY, 1962, p. 353.